Facile Composite Engineering to Boost Thermoelectric Power Conversion in ZnSb device

Vaskuri C. S. Theja[1], *Vaithinathan Karthikeyan*[2], *Sanjib Nayak*[3], *Kadir Ufuk Kandira*[2], *Dani S. Assi*[2], *Venkataramanan Kannan*[4], *Vellaisamy A. L. Roy*[2 *]

[1]Department of Materials Science and Engineering, City University of Hong Kong, Kowloon Tong, Hong Kong.

[2]Department of Electronics and Nanoscale Engineering, James Watt School of Engineering, University of Glasgow, Glasgow, United Kingdom.

[3]Department of Physics, Indian Institute of Technology Madras, Chennai, India.

[4]Department of Physics, Sri Chandrasekharendra Saraswathi Viswa Mahavidyalaya, Kanchipuram, India

*****Corresponding Author email: roy.vellaisamy@glasgow.ac.uk

ABSTRACT

Zinc antimonide (ZnSb) is one of the alternatives for commercial thermoelectric materials due to its non-toxic, low-cost, and earth-abundant nature. However, its simple crystal structure causes strong phonon vibrations, which enhance lattice thermal conductivity. In this work, we systematically studied the effect of **γ**-Al_2O_3 nano-inclusions on ZnSb. Our results show that composite engineering imparts lattice phonon scattering for reduced thermal conductivity and low-energy carrier filtering for enhanced Seebeck coefficient. The obtained figure of merit in the ZnSb+5% **γ**-Al_2O_3 sample at 673 K is nearly two-fold higher than the pristine sample. Our fabricated 2-leg ZnSb+5% **γ**-Al_2O_3 device displayed a power generation of 0.11 μW at ΔT of 200°C. Furthermore, adding **γ**-Al_2O_3 nano-inclusions improve the mechanical and thermal stabilities due to grain boundary hardening and dispersion strengthening. Overall, the addition of **γ**-Al_2O_3 nano-inclusions to ZnSb enhances the phonon scattering, reducing its thermal conductivity and improving mechanical and thermal stability significantly.

***Keywords*:** ZnSb; **γ**-Al_2O_3; nano-inclusion; phonon scattering; thermal conductivity

TOC Figure

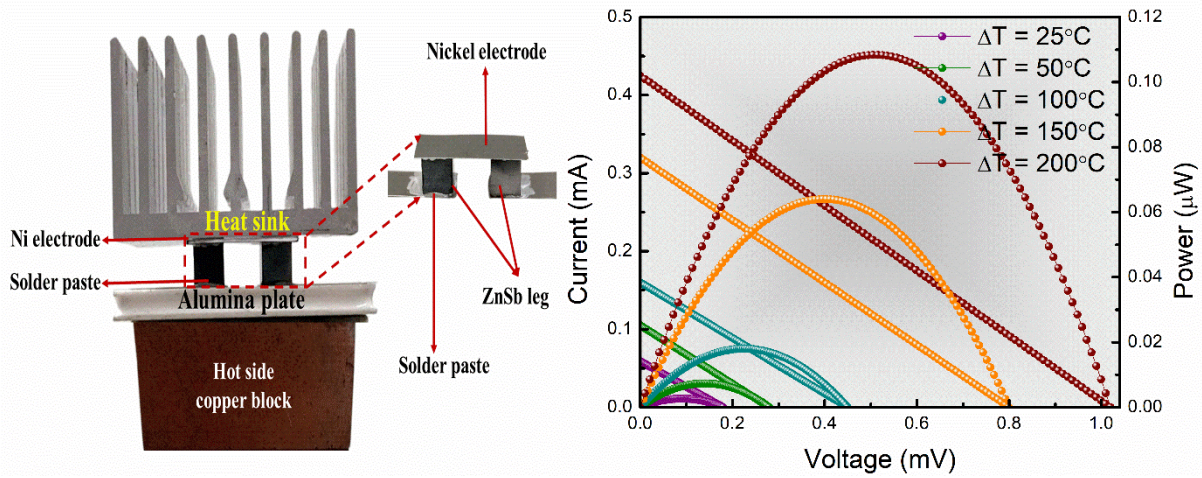
Nickel electrode
Heat sink
Ni electrode
Solder paste
Alumina plate
ZnSb leg
Solder paste
Hot side
copper block
ΔT = 25°C
ΔT = 50°C
ΔT = 100°C
ΔT = 150°C
ΔT = 200°C
Current (mA)
Power (μW)
Voltage (mV)
0.0
0.1
0.2
0.3
0.4
0.5
0.00
0.02
0.04
0.06
0.08
0.10
0.12
0.2
0.4
0.6
0.8
1.0

Introduction

At the global level, over 100 countries have set the goal to achieve net-zero carbon-based greenhouse gas emissions or neutrality targets[1]. To attain net-zero targets by 2050, heat recovery and energy conversion could play a significant role[2]. Solid-state thermoelectric conversion is one of the best alternative techniques for waste heat recovery applications. It is accounted that approximately over 7 Mtoe/year of waste heat can be recovered using thermoelectric devices[3]. Over 80% of generated industrial waste heat temperature ranges between 100°C to 300°C[4]. Commercial thermoelectric devices for direct conversion of waste heat to electricity are made of Bi_2Te_3; the latest research focussed on alternative materials, design, flexibility, optimization, and engineering[5–8]. However, Bi_2Te_3 is toxic, expensive, and applicable until near room temperature. Hence, the need for non-toxic, inexpensive materials such as metal antimonites is one of the better options for medium-temperature applications; on the other hand, their thermoelectric performance needs to be improved sustainably. Thermoelectric efficiency would be increased by enhancing the power factor or reducing thermal conductivity. However, the interdependent inverse relation between S, σ, and κ concerning carrier concentration creates hurdles in optimizing zT in a material[9]. This interdependency in the relationship can be understood from the Wiedemann-Franz law and Mott's formula shown in Eq. 1 and 2.

$$S = \frac{8\pi^2\kappa_B^2 T}{3eh^2} m_d^* \left(\frac{\pi}{3n}\right)^{2/3} \quad (1)$$

$$\kappa_e = L\sigma T = Lne\mu T \quad (2)$$

where L is Lorentz number, n is carrier concentration, and m_d^* is the density of state effective mass. Various strategies such as doping, nanostructuring, and defect engineering are being used and have improved thermoelectric conversion efficiency in different materials. In this aspect, nanostructuring is an easy and ideal technique to enhance zT without altering or deviating from the stoichiometry of the base thermoelectric compound[10]. Superlattices, quantum dots, nanowires, fine boundaries, and nano-inclusions are different techniques involved in the nanostructuring of thermoelectric materials[10]. Out of all these types, nano-inclusion techniques are inexpensive, easily controllable, facile synthesis, and practical approaches for commercialization[10].

The addition of nano-inclusions generates additional interfacial boundaries and fine grain boundaries, which primarily act as scattering points for acoustic phonons to reduce thermal

conductivity significantly[11,12]. Nano-inclusions are known to effectively scatter the phonons than charge carriers due to the mean free path of phonons being larger than charge carriers[13]. Insulating oxides as nano-inclusions improve the Seebeck coefficient inducing low-energy charge carrier scattering called the carrier-energy filtering mechanism. As an effect of the nano inclusion, the formation of carrier band bending near the interfacial boundaries is also observed[14–18][19,20]. As the size of nano inclusions is smaller than the mean free path of phonons and longer than charge carriers, they successfully scatter phonons and only filter low-energy charge carriers at the formed boundary interface [14,16]. "Phonon glass – electron crystal" model in thermoelectric materials is ideally possible by adding nano-inclusions[21,22]. Introducing nano-inclusions and nanograins formation through mechanical alloying favours the generation of high zT materials with improved mechanical and thermal stability[23]. Atomic defects formed during mechanical alloying scatter short-wavelength phonons, matrix-inclusion interfaces, and fine grain boundaries scatter long-wavelength phonons[24]. Both mechanical and thermal stability are crucial for thermoelectric materials; mainly, when used for high-temperature applications, they experience thermal stress[21,25]. Nano-inclusions also improve the composite material's phase and thermal and mechanical stability[25,26].

In the search for intermediate-temperature thermoelectric materials, Zinc antimonite (ZnSb) is a potential compound with an operating range between 500–700 K[14,20]. ZnSb is an inexpensive, non-toxic, and earth-abundant intermetallic thermoelectric material capable of being the future commercial non-toxic thermoelectric device[27,28]. The other advantages of the ZnSb semiconductor are its metallic characteristics, i.e., its phase stability and chemical durability. There are two possible types, stable thermoelectric phases formed by the elements Zn and Sb at room temperature, i.e., ZnSb (stable) and Zn_4Sb_3 (metastable)[29]. Zn_4Sb_3 has ultra-low thermal conductivity from its complex unit cell and produces high zT, which is precisely the opposite of ZnSb[30–32]. Zn_4Sb_3 has low thermal conductivity, making it favorable to attain higher zT than ZnSb; however, their thermal instability and Zn defects create a question to use it in commercial thermoelectric applications[14], while the advantage of ZnSb with the possibility for p-type/n-type via doping make them the best-suited material in the range of 300-500^{o}C[29,33] ZnSb is a stable phase, i.e., no phase transition is possible; however, its more unadorned orthorhombic crystal structure attributes to high thermal conductivity; therefore, its thermal conductivity should be optimized to improve zT[27]. The lattice part of the thermal conductivity depends on crystal structure and phonon transport; therefore, in a

simple crystal structure, ZnSb alloy is easily controlled by the addition of nanoparticles or extra boundaries to scatter the phonons.

Studies on ZnSb suggest that to synthesize nanograins samples; authors follow conventional direct melting followed by the mechanical alloying route to successfully form nanostructuring in the material to attain low thermal conductivity[34]. However, phase purity is critical when thermoelectric alloys are synthesized through melting, followed by an annealing route to achieve good thermoelectric performance. We often see this problem, i.e., forming either the Zn_4Sb_3 or Sb phases[34] However, for the first time, F. Tseng *et al.* successfully followed standard mechanical alloying and spark plasma sintering routes to form ZnSb alloy nanostructure [20]. Recently, Balasubramanian *et al.* synthesized ZnSb through mechanical alloying followed by a hot pressing route and obtained a fine grain and high phase purity ZnSb[35]. The synthesis route of mechanical alloying followed by hot pressing is a cost-effective technique for large-scale and obtaining fine grain structure in thermoelectric materials.

On the other hand, insulating oxide inclusions like Al_2O_3 effectively prove to enhance zT by reducing thermal conductivity and improving the Seebeck coefficient[13,25]. Al_2O_3 nano-inclusions also help enhance the mechanical and thermal stability of the composite[25]. In the present work, the effect of insulating γ-Al_2O_3 nano-inclusions and nano boundaries formed by mechanical alloying on ZnSb composite is studied. In this work, for the first time, we successfully reported the synthesis route of mechanical alloying followed by a hot pressing for ZnSb alloys without secondary (Zn_4Sb_3) phase formations. Adding γ-Al_2O_3 nano-inclusions significantly reduces thermal conductivity by interfacial phonon scattering and enhances the Seebeck coefficient by the low-energy carrier filtering effect. Realistically γ-Al_2O_3 nano-inclusions are observed to impart both mechanical and thermal stability to the ZnSb composite. Stable ZnSb, along with nanostructuring, is an effective strategy to attain high zT by lowering thermal conductivity and using it for commercial thermoelectric generator applications. Thus, we demonstrate an effective replacement for commercially available toxic Te, Se, and Pb-based thermoelectrical devices with environmentally benign ZnSb composite that exhibits high thermoelectric performance for waste heat recovery applications.

Materials and methods

Material synthesis and device fabrication

High purity elements of zinc powder (99% pure, Kurt. J. Lesker), antimony powder (99.999% pure, Kurt. J. Lesker), and γ-Al_2O_3 powder (99.99% pure, Sigma Aldrich) are weighted according to stoichiometry then mixed and grounded thoroughly using an agate mortar and pestle. Polycrystalline ZnSb + x% γ-Al_2O_3 nano-inclusions of various nominal compositional atomic percentages (x = 0, 1, 3, and 5) were fabricated through conventional mechanical alloying, i.e., high-energy ball milling followed by hot pressing consolidation technique. First, the nominal compositions with corresponding nano-inclusions concentration were mechanically alloyed in a planetary ball mill at 300 rpm for 24 hours using zirconia balls with a powder-to-ball ratio of 1:20. Then ball-milled powders are compacted into pellets by hot pressing in a mold of die diameter of 15 mm at 400 °C under uniaxial pressure of 120 MPa for 10 minutes to produce compacted and high-densified samples. ZnSb + 5% γ-Al_2O_3 powder was hot-pressed using a square die to fabricate two p-type legs of 8 mm length and 4×4 mm cross-section. The fabricated legs are interconnected in electrical series using nickel electrodes and solder paste; the hot side is joined to the alumina plate using carbon tape. The complete fabricated thermoelectric device, the heat sink attached on the cold side, and the heating copper block on the hot side are shown in Fig. 2i.

Structural characterization

Structural and phase analysis were investigated using the powder X-ray diffraction method in Bruker D2 Phaser instrument using Cu K_α radiation of wavelength 1.5406 Å and Lynxeye detector. In all samples, diffraction patterns were measured from 2θ of 10 to 90° with a step size of 0.02°. Then, the lattice parameter and lattice volume were calculated from the obtained XRD data using Bragg's law. The Raman spectra were recorded using an excitation HeNe laser wavelength of 532 nm in Renishaw Raman Spectroscopy 2000 instrument to understand the phase formations using molecular bonding-related vibrational intensities. Low magnification fractography was conducted using Philips scanning electron microscope (SEM) assisted EDAX and elemental mapping to understand the presence and distribution of Al_2O_3 nano-inclusions within the matrix phase. Hardness measurements are conducted on finely polished test samples using a Vickers hardness tester of 5 kgf load with 10 seconds dwell time at room temperature. TGA and DSC were performed on all the samples in a Simultaneous Thermal Analyser of PerkinElmer STA6000.

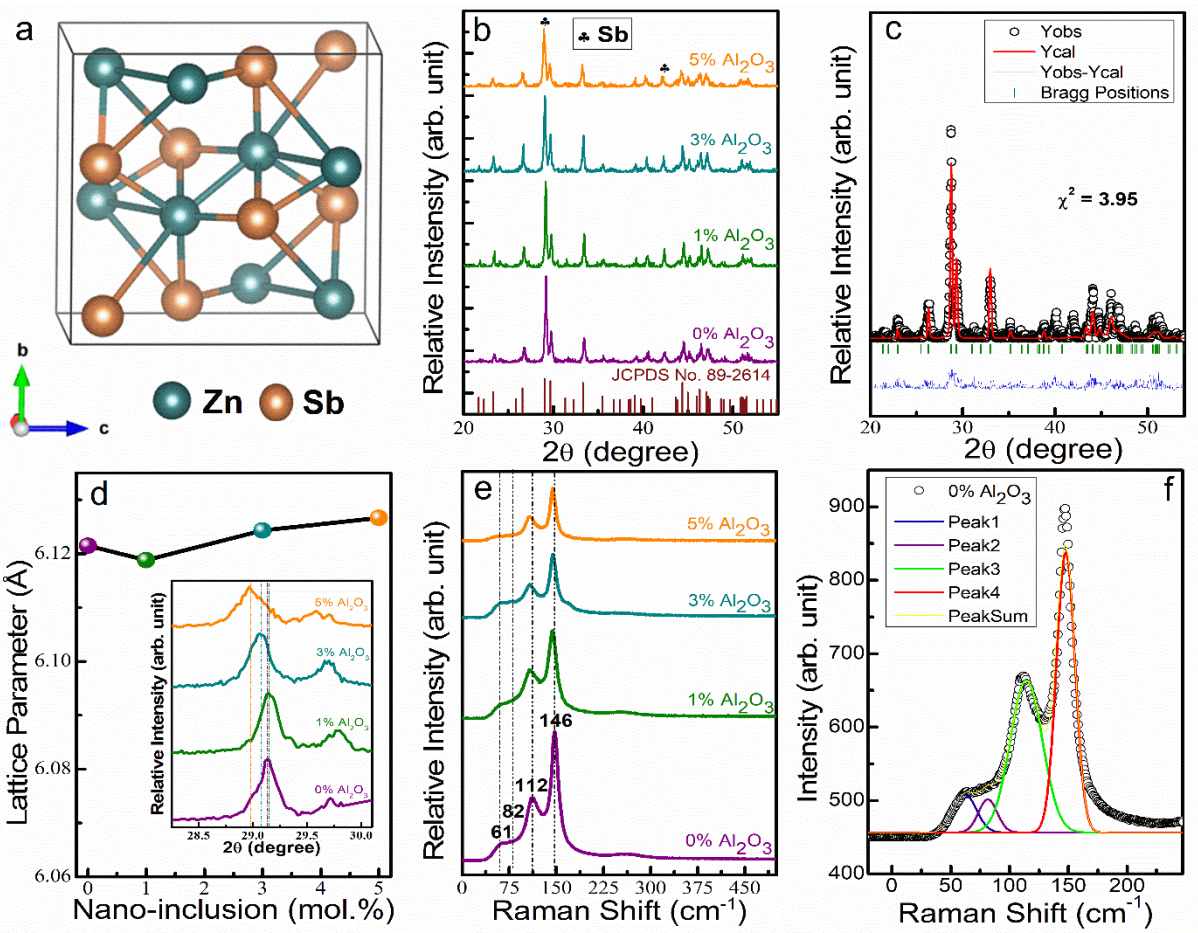

Figure 1 (a) Cystal structure, (c) Rietveld refinement, and (f) Deconvoluted Raman peaks of pristine ZnSb, (b) XRD, (d) lattice parameter with inset showing peak shift, and (e) Raman spectra of the samples ZnSb+x% γ-Al_2O_3 samples (x = 0, 1, 3, and 5).

Thermoelectric characterization

Thermoelectric measurements of σ, S, and κ were conducted from room temperature to 673 K with 50 K intervals. The charge transport properties, i.e., carrier concentration and mobility, were measured using the Lakeshore Hall measurement system in the magnetic field range of -2T to +2T at room temperature. Electrical conductivity and Seebeck coefficient were calculated using standard four-probe direct current measurement in SBA 458 Nemesis (Netzsch) apparatus under argon atmosphere from room temperature to 673 K. In all the samples, Fermi level (E_f) over the temperature range and the density of states associated effective mass (m_d^*) and the effective density of states (*eDOS*) at room temperature is theoretically calculated using measured carrier concentration and Seebeck coefficient. Thermal diffusivity values were measured on 12.7 mm diameter with 3 mm thickness disk samples in Netzsch LFA 467 machine using a laser flash method under an inert atmosphere. The densities of the obtained

samples were calculated using the standard Archimedes method. Thermal conductivities were measured automatically in Netzsch-assisted software using the standard formula $\kappa = \rho\alpha C_p$ Where ρ is the density of the sample, C_p is specific heat, and α is thermal diffusivity. Finally, the power factor ($S^2\sigma$) and the dimensionless figure-of-merit were calculated using the obtained Seebeck coefficient, electrical, and thermal conductivity values. Temperature-dependent thermoelectric device performance was acquired by the sweeping load resistance. The corresponding change in voltage, current, and power was recorded using the Keithley 6517A Electrometer and hot side temperature using a K-type thermocouple.

Results and discussion

As shown in Fig. 1a, ZnSb possesses an orthorhombic crystal structure with tuneable semiconducting properties, crystallizing with the *P/bca* space group and the bandgap of approximately ~ 0.86 eV[36]. All the ZnSb + x% γ-Al_2O_3 (x = 0, 1, 3, and 5) samples are successfully hot pressed, with densification reaching approximately 90% in all samples. However, nano-inclusion reduces the density almost linearly due to the formation of back stress against sintering pressure between the matrix and inclusion interface. The low-density Al_2O_3 phase also contributes to the reduced density[11]. Milling parameters do not influence the formation of the ZnSb phase without any secondary Zn_4Sb_3 phase, mainly due to the high stability of the ZnSb phase[12]. As shown in Fig. 1b, in XRD, along with ZnSb peaks, we also observed the two peaks of the Sb phase. No peaks related to the γ-Al_2O_3 nano-inclusion phase are observed due to the low concentration of γ-Al_2O_3 added[26]. As shown in Fig. 1c and Fig. S1, we conducted the Rietveld refinement to evaluate the lattice parameter change in all the samples. The inset of Fig. 1d showcases the left shift of the high-intensity XRD peak with increasing nano-inclusions concentration, which indicates lattice expansion. As shown in Fig. 1d, the change in the lattice parameter (a) with increasing concentration of γ-Al_2O_3 nano-inclusions is observed; however, it is complex to consider this change attributed to nano-inclusions due to the presence of Sb atoms in all samples. The grain size is calculated from the XRD data using Eq. 3, called the Scherrer formula. The results shown in Table 1 indicate the reduction in grain size with increasing the concentration of γ-Al_2O_3 nano-inclusions. Ball milling with harder nano-inclusions reduces the grain size of the matrix ZnSb phase and increases the number of grain boundaries[23,29]. As shown in Fig. 1e, Raman peak intensities are reduced by adding γ-Al_2O_3 nano-inclusions, which means the added nano-inclusions successfully reduce the molecular lattice vibrations. As shown in Fig. 1f, deconvoluted Raman

peaks observed at 61, 82, and 146 cm^{-1} indicate the presence of the ZnSb phase along with secondary Sb phase (peak at 112 cm^{-1}) vibration modes in all samples[35,37]. The secondary electron SEM micrograph shown in Fig. 2a reveals the surface morphology of the pristine ZnSb sample with apparent porosity. As shown in Fig. 2b, the backscattered electron SEM image reveals the γ-Al_2O_3 nano-inclusions uniform distribution in the 5% γ-Al_2O_3 composite sample. Fig. 2g shows the energy dispersive spectrum showing Al nano-inclusions in the 5% γ-Al_2O_3 composite sample without impurity peaks. Fig. 2(c-f) depicts the corresponding elemental mapping with the distribution of homogeneous Al nano-inclusion. From Fig. 2d and 2f, it is clearly understood that Zn is relatively thin than Sb, which is due to the Zn loss during the ball milling process; the presence of the Sb phase is already identified by XRD and Raman.

$$D = \frac{0.9\lambda}{\beta \cos\theta} \quad (3)$$

Where D is grain size in nm, β is FWHM of an XRD peak, θ is half of the diffraction angle in radians and λ is the wavelength of the XRD source in nm.

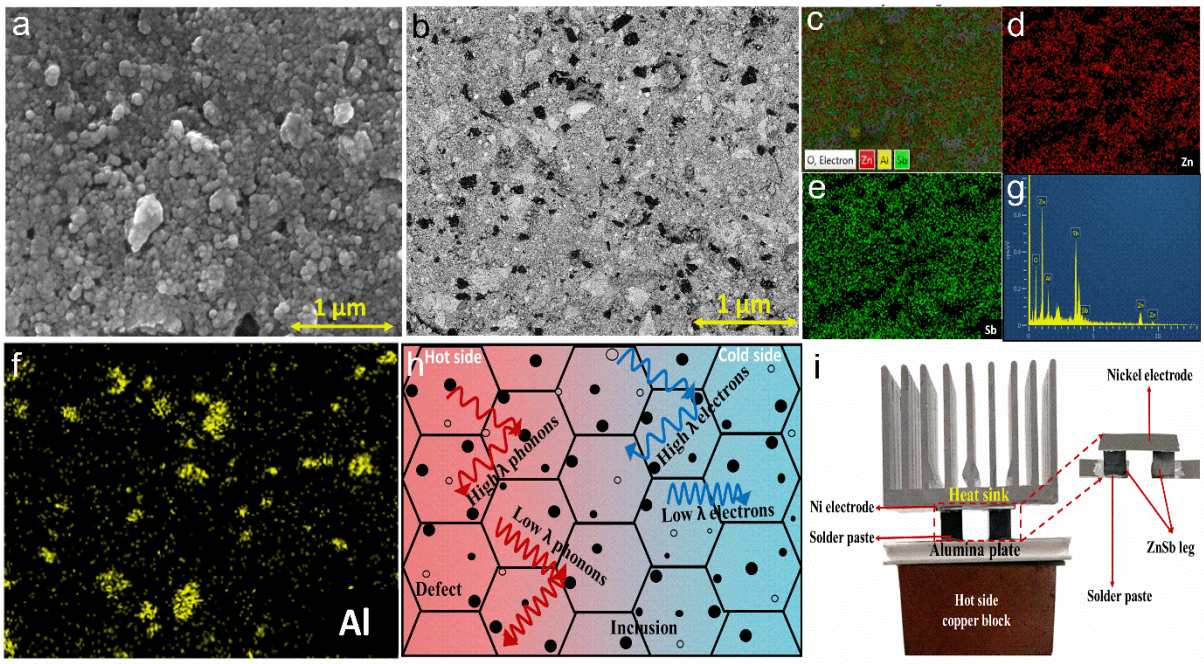

Figure 2 (a) Surface morphology of pristine sample, (b) SEM BSE micrograph, (c-f) elemental mapping, and (g) EDAX of the 5% γ-Al_2O_3 composite sample, (h) schematic carrier scattering diagram , (i) device construction.

Temperature-dependent electrical resistivity is measured in all the samples shown in Fig. 3a. From the plots; it is observed that all the samples show non-degenerate semiconductor behavior of intrinsic carrier excitation at a high temperature significantly above 400 K. Electrical

conductivity is reduced by the addition of insulating γ-Al_2O_3 nano-inclusions due to the solid potential charge carrier scattering, which reduces furthermore with increasing the concentration of nano-inclusions[11]. Along with the scattering of carriers, increased porosity also contributes to the electrical conductivity reduction[11]. We calculated the carrier concentration and mobility in all samples at room temperature from the Hall effect results, as shown in Fig. 3f. Positive signed carrier concentration values measured using Hall Effect suggest *p*-type electrical transport behavior in all samples. The obtained carrier concentration is within the optimum range (i.e., 10^{20} to 5×10^{20} cm^{-3}) to achieve maximum power factor in all the samples[38]. Carrier concentration and mobility are reduced linearly by adding γ-Al_2O_3 nano-inclusions, which confirms the γ-Al_2O_3 nano-inclusions effectively scattering the ZnSb charge carriers. In-coherent interfacial boundaries formed by the γ-Al_2O_3 lessen the mobility of the ZnSb carriers[39]. Added nano-inclusions scatter the medium to high wavelength, i.e., reduction in overall carrier concentration, which is the primary reason for reduced electrical conductivity. The added nano-inclusions also reduce the mobility of the carriers by forming insulating boundaries for matrix charge carrier transport[40]. Increased porosity by added insulating γ-Al_2O_3 nano-inclusions also contributes to the reduced electrical conductivity[18,25].

The single parabolic band (SPB) model is a simple and effective approach to finding and understanding the fundamental charge transport properties from the calculated experimental thermoelectric parameters and carrier concentration[41]. SPB model was used to find the reduced Fermi level (E_f), density of states effective mass (m_d^*) and effective density of states $eDOS$) are determined from the equations 4, 5 and 6[9,41]:

$$S = \frac{k_B}{e}\left[\frac{(\lambda+2)F_{\lambda+1}(\eta)}{(\lambda+1)F_\lambda(\eta)} - \eta\right] \quad (4)$$

$$m_d^* = \frac{h^2}{2k_B T m_0}\left(\frac{p}{4\pi F_{1/2}(\eta)}\right)^{2/3} \quad (5)$$

$$eDOS = 2 \times \left(\frac{2\pi m_0 m_d^* k_B T}{h^2}\right)^{3/2} \quad (6)$$

Where, $\eta = \frac{E_f}{k_B T}$ is reduced chemical potential, λ is scattering parameter, m_0 is rest mass of electron and $F_i(\eta)$is the Fermi integral of order *i*, $F_i(\eta) = \int_0^\infty \frac{\epsilon^i d\epsilon}{1+Exp[\epsilon-\eta]}$. We considered the λ as zero, due to the dominance of the acoustic phonon scattering[42,43]. Fermi level is reduced by the addition of γ-Al_2O_3 nano-inclusions, which is shown in Fig. 5b, indicating the Fermi

level moves towards the conduction band attributed to reduced carrier hole concentration. The calculated effective density of states (*eDOS*), which is in the order of 10^{19} $cm^{-3,}$ and the density

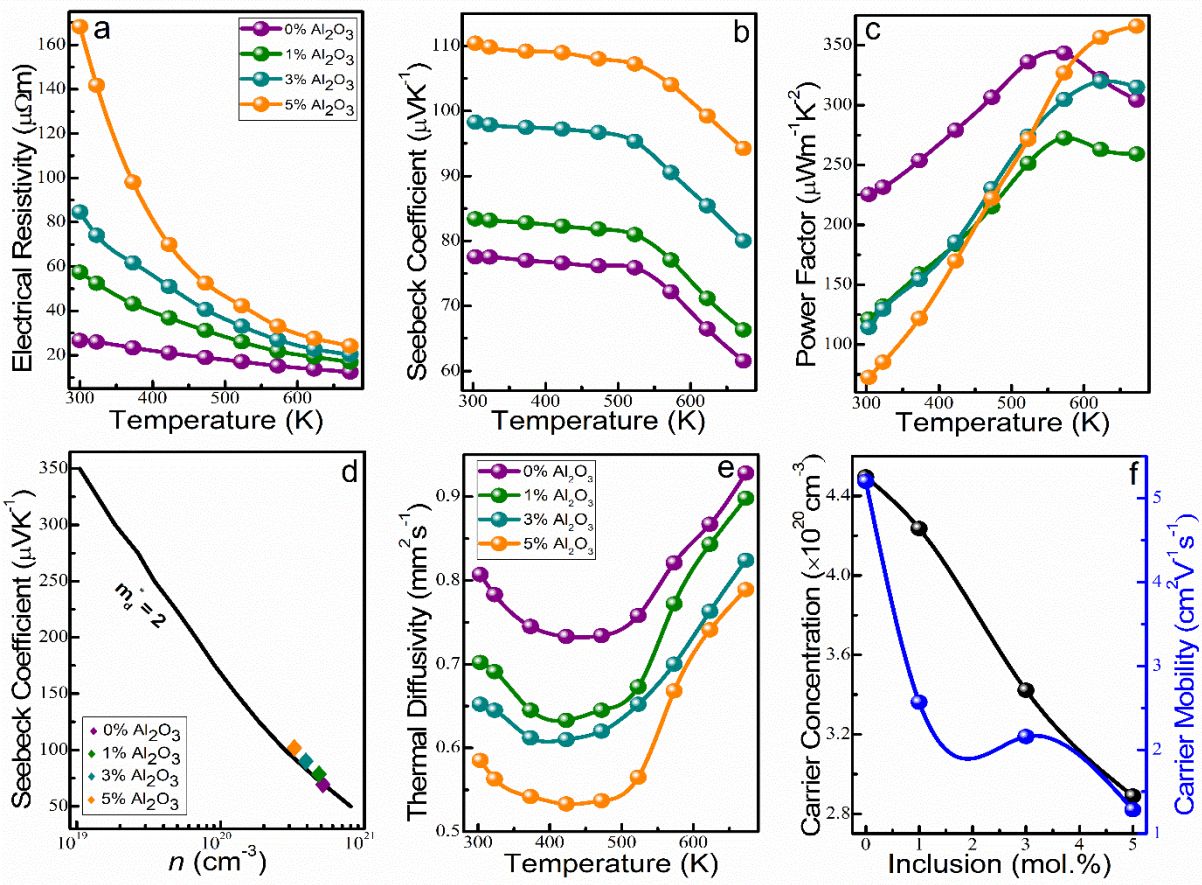

Figure 3 (a) Electrical resistivity, (b) Seebeck coefficient, (c) Power factor (d) Pisarenko relation, (e) thermal diffusivity and, (f) Room temperature carrier concentration and mobility of the samples ZnSb+x% γ-Al_2O_3 samples (x = 0, 1, 3, and 5).

of states' effective mass (m_d^*) which is greater than two in all the samples at room temperature mentioned in Table 1 indicating the increase in both the parameter by the addition of γ-Al_2O_3 nano-inclusions proportionally attributed to the enhancement in Seebeck coefficient.

Temperature-dependent Seebeck coefficient is shown in Fig. 3b, representing the positive thermopower values confirming the p-type semi-conductive behavior in all the samples. All samples follow the same trend, which is Seebeck coefficient slightly reducing (almost constant) from 303 to 573 K then reducing faster up to 673 K. The Seebeck coefficient is increased from pristine to 1 to 3 to 5% sample due to the carrier-energy filtering mechanism by the addition of γ-Al_2O_3 nano-inclusions[40]. At high temperatures, reduction in the Seebeck coefficient is mainly due to the activation of intrinsic minority charge carriers, i.e., electrons contribute to the bipolar effect[19,31]. Measured Seebeck coefficient values are confirmed by

the Pisarenko relation, which also confirmed by the theoretically calculated effective mass increased with increasing nano-inclusion concentration[44–48]. As shown in Fig. 2h, added γ-Al_2O_3 nano-inclusions scatter the low-energy charge carriers, contributing to the Seebeck coefficient enhancement. As shown in Fig. 3c the power factor is reduced by the addition of nano-inclusions compared to pristine samples except in the 5% γ-Al_2O_3 sample at high temperature. The reduced power factor is mainly attributed to the reduced electrical

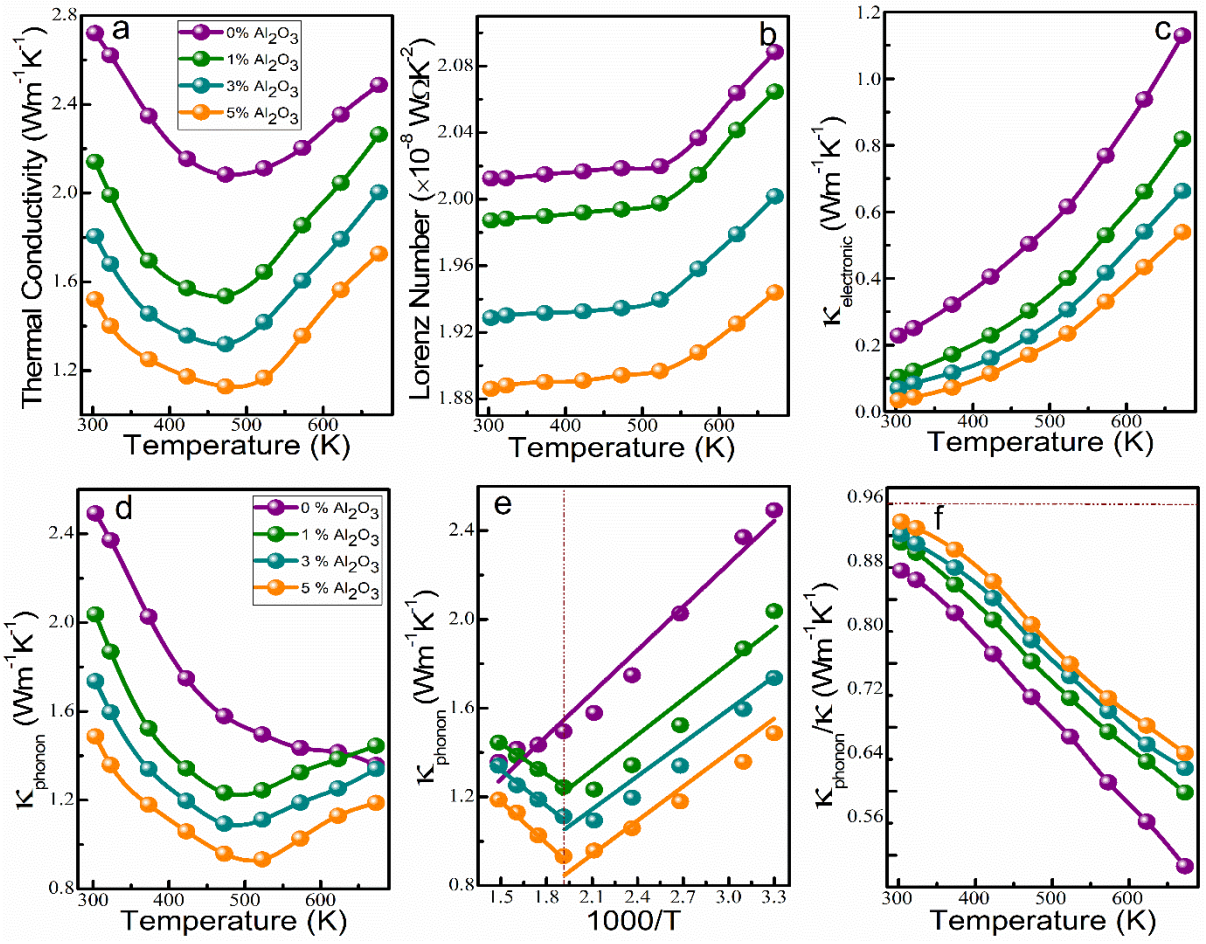

Figure 4 Temperature dependent (a) Thermal conductivity, (b) Lorenz number, (c) Electronic thermal conductivity, (d) Phonon thermal conductivity, (e) κ_{phonon} vs 1000/T and, (f) κ_{phonon}/κ of the samples ZnSb+x% γ-Al_2O_3 samples(x = 0, 1, 3, and 5).

conductivity that dominates the improved Seebeck coefficient by the addition of γ-Al_2O_3 nano-inclusions. The plotted Pisarenko relation for effective mass perfectly matches and validates the obtained experimental S and carrier concentration as shown in Fig. 3d.

Temperature-dependent thermal conductivity shows a similar trend in all the samples, as shown in Fig. 4a. In all the samples, thermal conductivity decreased rapidly up to 473 K and then continued to increase up to 673 K. Increased secondary carriers at high temperature contribute

to the electronic part of the thermal conductivity to increase overall thermal conductivity at a high temperature called bipolar effect[20]. Thermal conductivity is successfully reduced from pristine to 1% to 3% to 5% γ-Al_2O_3, by the addition of homogenous γ-Al_2O_3 nano-inclusions, as shown in the SEM Fig. 2f. Phonons of various wavelengths, especially mid to long wavelengths, are scattered by the added γ-Al_2O_3 nano-inclusions, which are major carriers for thermal conductivity, as shown in Fig. 2h. Added γ-Al_2O_3 nano-inclusions reduced the mean free path of phonons in the composite to reduce the lattice thermal conductivity. Along with added γ-Al_2O_3 nano-inclusions interface boundaries, fine-grain boundaries, low γ-Al_2O_3 thermal conductivity, and defects formed during mechanical alloying contribute to reducing lattice thermal conductivity[39,49]. Nano-inclusions effectively scatter mid to high wavelength phonons more than short-wavelength phonons. However, atomic-scale defects and fine grain boundaries scatter short-wavelength phonons; therefore, γ-Al_2O_3 added samples scatter a broad spectrum of phonon wavelengths.

Table 1 The grain size, density, porosity, Fermi level, effective mass, and effective DOS of the ZnSb+x% γ-Al_2O_3 samples (x= 0, 1, 3, and 5).

Inclusion (*mol.%*)	**Grain size (*nm*)**	**Density (*g/cc*)**	**Porosity (*%*)**	**Fermi level (*meV*)**	**Effective mass**	**Effective DOS ($10^{19}cm^3$)**
0	40.02	5.68	10.24	87	2.10	7.79
1	36.26	5.62	11.11	79	2.18	8.25
3	31.73	5.51	12.60	64	2.25	8.64
5	23.07	5.40	14.10	53	2.29	8.85

The thermal conductivity in a pristine ZnSb sample of $2.5\,W/mK$ is significantly high compared to the thermal conductivity of Zn_4Sb_3 alloy. High porosity levels, as mentioned in Table 1, i.e., around 10% and ZnSb simple unit cell structure, as shown in Fig. 1a, are detrimental to thermal transport resistance and strongly affect obtained thermal conductivity and resultant thermoelectric performance. Total thermal conductivity is a sum of the contribution from charge carriers (electrical part) and phonons (lattice part), i.e., $\kappa_{total} =$

$\kappa_{electrical} + \kappa_{lattice}$ Where the electrical part of the thermal conductivity is calculated from equation 2. Lorenz number is calculated from the measured Seebeck coefficient using the formula $L = 1.5 + \exp(-|S|/116)$ with units of 10^{-8} $W\Omega K^{-2}$ where S is in μV/K suggested by Kim *et al.* [50] shown in Fig. 4b. κ_e and κ_p are plotted concerning temperature, as shown in Figs. 4c and 4d, both parts of the thermal conductivity reduced by the addition of γ-Al_2O_3 nano-inclusions contribute to the total thermal conductivity reduction. The contribution of κ_e towards total κ is high because of the presence of metallic Sb atoms, which we observed from the XRD. In all samples concerning temperature, thermal excitation of minority carriers by increasing the temperature contribute towards κ_e enhancement. However, by the addition of γ-Al_2O_3 nano-inclusions, κ_e was reduced compared to pristine samples due to the reduction of σ. Coming to phonon thermal conductivity, in all the samples, κ_p decreased rapidly up to 473 K. In pristine sample, decrease in κ_p continued up to 673 K, however in composite samples thermal conductivity started increasing above 473 K until 673 K. As shown in Fig. 4e, κ_l is plotted against 1000/T, which indicates the phonon – phonon scattering dominated from room temperature to 573 K due to the Umklapp process. However, above 573 K, the slope of the linear relationship becomes reverse, which indicates the dominance of bipolar diffusion from excited minority carriers in the composite samples [51,52]. Phonon's contributions toward total thermal conductivity are higher than electrons, as shown in Fig. 4f.

The figure-of-merit values shown in Fig. 5a suggest the zT is improved by the addition of γ-Al_2O_3 nano-inclusions. To assure the accuracy of the evaluated figure-of-merit, we measured the thermoelectric parameters multiple times, as shown in Fig. S2. Both pristine and 1% γ-Al_2O_3 added samples showing nearly the same zT at all temperatures means there is no significant enhancement by adding 1% γ-Al_2O_3 nano-inclusions. The maximum zT obtained is 0.14 in the 5% γ-Al_2O_3 samples at 673 K, which is almost a two-fold improvement compared to the pristine sample. One of the primary reasons for low zT in these samples is the relatively high thermal conductivity compared to other reported ZnSb alloys. The high percentage of porosity of around 10% after hot pressing is one of the major causes of charge-carrier transport resistance. Thermoelectric alloys require very high densification or solidity to acquire good thermoelectric and stability properties; otherwise, they show a detrimental effect on charge-carrier transportation and negatively impact the figure-of-merit. The complete structure of the designed 2-leg device, hot-side copper block, and cold-side aluminum heat sink is shown in Fig. 2i. The designed 2-leg, 5% γ-Al_2O_3 highlighted the power of 0.11 μW at the temperature difference of 200°C, as shown in Fig. 5c.

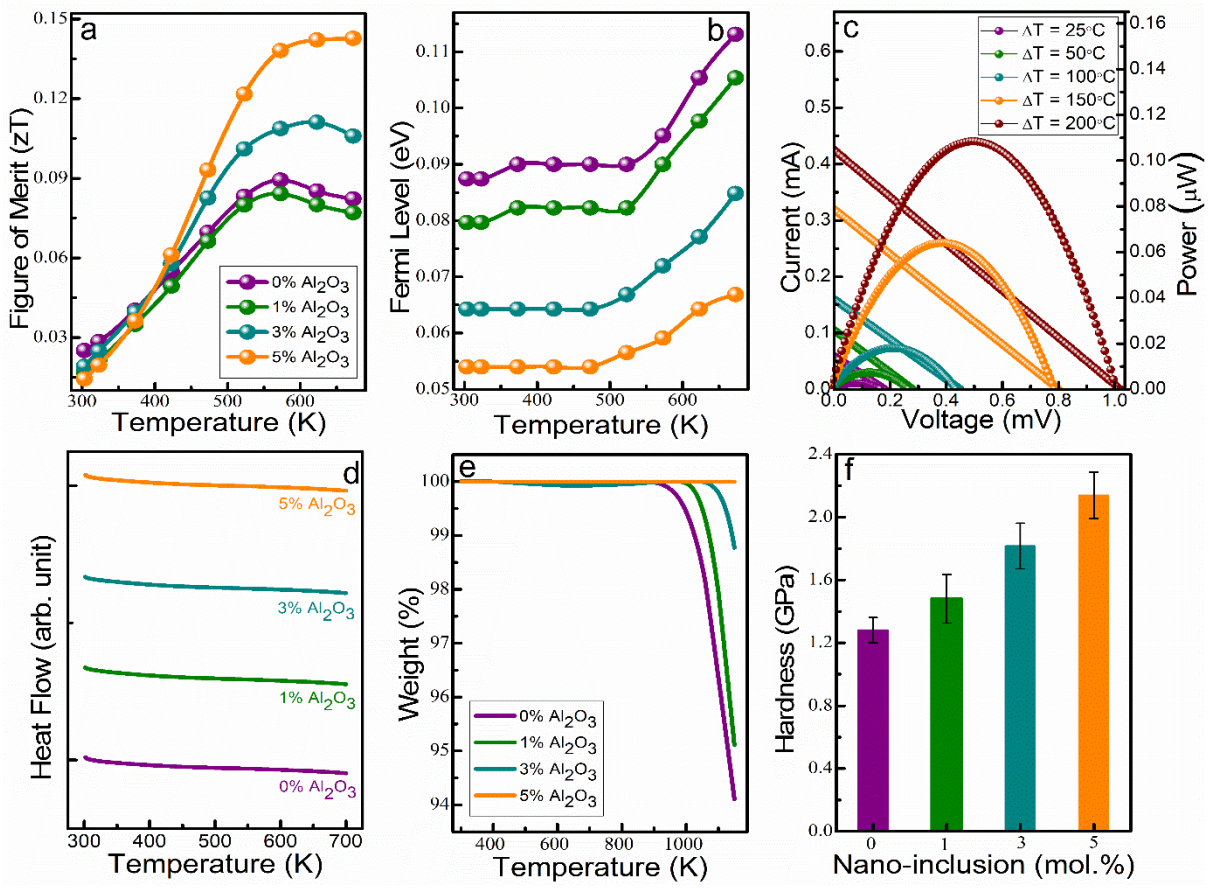

Figure 5 (a) Figure-of-merit, (b) Fermi level, (c) power performance of the device, (d) DSC phase stability, (e) TGA thermal stability and, (f) Vickers hardness of the ZnSb+x% γ-Al_2O_3 samples (x = 0, 1, 3, and 5).

To understand the phase stability, plotted DSC curves for all the samples up to 700 K as shown in Fig. 5d. From the DSC results, it is clear that there are no peaks in the curves, which indicates the high phase stability of ZnSb and which is also maintained by the addition of inclusions. Thermal stability is improved by the added γ-Al_2O_3 nano-inclusions, which are shown in Fig. 5e. High mechanical strength is a mandatory requirement for the commercialization of high-performance thermoelectric materials, which improved by the addition of γ-Al_2O_3 nano-inclusions. Mechanical stability is one of the primary parameters to improve the lifetime of thermoelectric devices during their application period. Mechanical stability measured by Vickers hardness in the ZnSb samples is enhanced by the addition of γ-Al_2O_3 nano-inclusions, as shown in the inset of Fig. 5f, where hardness increases from 130 HV in the pristine to 218 HV in 5% γ-Al_2O_3 samples linearly. As mentioned in Table 1, nano-grain size and Fig. 2f, homogenous Al_2O_3 dispersions helps in mechanical strengthening. The added nano-inclusions improved the mechanical strength through grain boundary hardening and dispersions hardening

from the nano-inclusion secondary phase[19]. Therefore, our study providing the clear insights on the nanocomposite engineering by γ-Al_2O_3 inclusions helps in improving the thermoelectric performance, mechanical and thermal stability of the ZnSb material. It opens up gates in new direction to build and improve the ZnSb thermoelectric performance and making it as potential candidate to replace the commercial Bi_2Te_3 thermoelectric device materials.

Conclusion

In this study, ZnSb + x% γ-Al_2O_3 (x = 0, 1, 3, and 5) alloys are successfully synthesized through facile mechanical alloying followed by hot pressing. The addition of γ-Al_2O_3 nano-inclusions reduces both carrier concentration and mobility, reducing overall electrical conductivity. Seebeck coefficient is enhanced by the addition of γ-Al_2O_3 nano-inclusions, mainly attributed to the carrier-energy filtering effect, i.e., scattering of low-energy carriers by band bending near the interfacial boundaries. Power factor is reduced in γ-Al_2O_3 nano-inclusion added samples, especially in 1% and 3% samples, due to the reduction in electrical conductivity dominates the increase in Seebeck coefficient. Thermal conductivity is reduced by the addition of γ-Al_2O_3 nano-inclusions in all samples due to the strong phonon scattering. A high porosity level contributes to charge carrier transport resistance, and ZnSb's uncomplicated structure contributes to thermal transport resistance synergistically, showing a strong negative effect on obtained overall zT. We reported the maximum zT obtained is 0.14 in 5% γ-Al_2O_3 added samples, which is almost two-fold to pristine sample at 673 K. The 2-leg coupled ZnSb+5% γ-Al_2O_3 device displayed the maximum power of 0.11 μW at ΔT of 200°C. With the addition of γ-Al_2O_3 nano-inclusions, the composite's thermal and mechanical stability improved. Our study demonstrates that nanocomposite is a simple and effective solution to enhance the zT and strength of ZnSb material to make a potential alternative for Te-based devices.

Declaration of Competing Interest

The authors declare that they have no known competing financial interests or personal relationships that could have appeared to influence the work reported in this paper.

Acknowledgments

We acknowledge grants from the Research Grants Council of Hong Kong Special Administrative Region Project No: T42-103/16N. We are thankful to Dr. Abhijit Pramanick, Department of Materials Science and Engineering, City University of Hong Kong to access his lab facility during this project.

References

[1] H.L. van Soest, M.G.J. den Elzen, D.P. van Vuuren, Net-zero emission targets for major emitting countries consistent with the Paris Agreement, Nat Commun. 12 (2021) 1–9. https://doi.org/10.1038/s41467-021-22294-x.

[2] The Royal Society, Low-carbon heating and cooling : overcoming one of world ' s most important net zero challenges, (2021) 1–12.

[3] P. Pichanusakorn, P. Bandaru, Nanostructured thermoelectrics, Materials Science and Engineering R: Reports. 67 (2010) 19–63. https://doi.org/10.1016/j.mser.2009.10.001.

[4] R. Freer, A. V. Powell, Realising the potential of thermoelectric technology: A Roadmap, J Mater Chem C Mater. 8 (2020) 441–463. https://doi.org/10.1039/c9tc05710b.

[5] Z.H. Zheng, X.L. Shi, D.W. Ao, W. di Liu, M. Li, L.Z. Kou, Y.X. Chen, F. Li, M. Wei, G.X. Liang, P. Fan, G.Q. (Max) Lu, Z.G. Chen, Harvesting waste heat with flexible Bi2Te3 thermoelectric thin film, Nat Sustain. 6 (2023) 180-191. https://doi.org/10.1038/s41893-022-01003-6.

[6] T. Cao, X.L. Shi, Z.G. Chen, Advances in the design and assembly of flexible thermoelectric device, Prog Mater Sci. 131 (2023) 101003. https://doi.org/10.1016/j.pmatsci.2022.101003.

[7] W.Y. Chen, X.L. Shi, J. Zou, Z.G. Chen, Thermoelectric coolers for on-chip thermal management: Materials, design, and optimization, Materials Science and Engineering R: Reports. 151 (2022) 100700. https://doi.org/10.1016/j.mser.2022.100700.

[8] D.W. Ao, W. di Liu, Y.X. Chen, M. Wei, B. Jabar, F. Li, X.L. Shi, Z.H. Zheng, G.X. Liang, X.H. Zhang, P. Fan, Z.G. Chen, Novel Thermal Diffusion Temperature Engineering Leading to High Thermoelectric Performance in Bi_2Te_3-Based Flexible Thin-Films, Advanced Science. 9 (2022) 2103547. https://doi.org/10.1002/advs.202103547.

[9] V. Karthikeyan, T. Li, B. Medasani, C. Luo, D. Shi, J.C.K. Wong, K.H. Lam, F.C.C. Ling, V.A.L. Roy, Defect and Dopant Mediated Thermoelectric Power Factor Tuning in β-Zn_4Sb_3, Adv Electron Mater. 6 (2020) 1–9. https://doi.org/10.1002/aelm.201901284.

[10] A.J. Minnich, M.S. Dresselhaus, Z.F. Ren, G. Chen, Bulk nanostructured thermoelectric materials: Current research and future prospects, Energy Environ Sci. 2 (2009) 466–479. https://doi.org/10.1039/b822664b.

[11] F. Li, X. Huang, Z. Sun, J. Ding, J. Jiang, W. Jiang, L. Chen, Enhanced thermoelectric properties of n-type Bi_2Te_3-based nanocomposite fabricated by spark plasma sintering, J Alloys Compd. 509 (2011) 4769–4773. https://doi.org/10.1016/j.jallcom.2011.01.155.

[12] R. Pothin, R.M. Ayral, A. Berche, D. Granier, F. Rouessac, P. Jund, Preparation and properties of ZnSb thermoelectric material through mechanical-alloying and Spark Plasma Sintering, Chemical Engineering Journal. 299 (2016) 126–134. https://doi.org/10.1016/j.cej.2016.04.063.

[13] K.T. Kim, G.H. Ha, Fabrication and enhanced thermoelectric properties of alumina nanoparticle-dispersed $Bi_{0.5}Sb_{1.5}Te_3$ matrix composites, J Nanomater. 2013 (2013) 1–7. https://doi.org/10.1155/2013/821657.

[14] K. Berland, X. Song, P.A. Carvalho, C. Persson, T.G. Finstad, O.M. Løvvik, Enhancement of thermoelectric properties by energy filtering: Theoretical potential and experimental reality in nanostructured ZnSb, J Appl Phys. 119 (2016) 1–10. https://doi.org/10.1063/1.4944716.

[15] J. Li, Q. Tan, J.F. Li, D.W. Liu, F. Li, Z.Y. Li, M. Zou, K. Wang, BiSbTe-based nanocomposites with high ZT: The effect of SiC nanodispersion on thermoelectric properties, Adv Funct Mater. 23 (2013) 4317–4323. https://doi.org/10.1002/adfm.201300146.

[16] S. V. Faleev, F. Léonard, Theory of enhancement of thermoelectric properties of materials with nanoinclusions, Phys Rev B Condens Matter Mater Phys. 77 (2008) 214304. https://doi.org/10.1103/PhysRevB.77.214304.

[17] D.L. Medlin, G.J. Snyder, Interfaces in bulk thermoelectric materials. A review for Current Opinion in Colloid and Interface Science, Curr Opin Colloid Interface Sci. 14 (2009) 226–235. https://doi.org/10.1016/j.cocis.2009.05.001.

[18] C. Gayner, Y. Amouyal, Energy Filtering of Charge Carriers: Current Trends, Challenges, and Prospects for Thermoelectric Materials, Adv Funct Mater. 30 (2020) 1–17. https://doi.org/10.1002/adfm.201901789.

[19] B. Madavali, H.S. Kim, K.H. Lee, S.J. Hong, Enhanced Seebeck coefficient by energy filtering in Bi-Sb-Te based composites with dispersed Y_2O_3 nanoparticles, Intermetallics (Barking). 82 (2017) 68–75. https://doi.org/10.1016/j.intermet.2016.11.002.

[20] F. Tseng, S. Li, C. Wu, Y. Pan, L. Li, Thermoelectric and mechanical properties of ZnSb/SiC nanocomposites, J Mater Sci. 51 (2016) 5271–5280. https://doi.org/10.1007/s10853-016-9830-x.

[21] M.G. Kanatzidis, Nanostructured thermoelectrics: The new paradigm?, Chemistry of Materials. 22 (2010) 648–659. https://doi.org/10.1021/cm902195j.

[22] G.J. Snyder, M. Christensen, E. Nishibori, T. Caillat, B.B. Iversen, Disordered zinc in Zn_4Sb_3 with phonon-glass and electron-crystal thermoelectric properties, Nat Mater. 3 (2004) 458–463. https://doi.org/10.1038/nmat1154.

[23] T. Wang, H. Wang, W. Su, J. Zhai, G. Yakovleva, X. Wang, T. Chen, A. Romanenko, C. Wang, Simultaneous enhancement of thermoelectric and mechanical performance for SnTe by nano SiC compositing, J Mater Chem C. 8 (2020) 7393–7400. https://doi.org/10.1039/d0tc00572j.

[24] W. Kim, J. Zide, A. Gossard, D. Klenov, S. Stemmer, A. Shakouri, A. Majumdar, Thermal conductivity reduction and thermoelectric figure of merit increase by embedding nanoparticles in crystalline semiconductors, Phys Rev Lett. 96 (2006) 1–4. https://doi.org/10.1103/PhysRevLett.96.045901.

[25] P. Wen, H. Mei, P. Zhai, B. Duan, Effects of nano-α-Al_2O_3 dispersion on the thermoelectric and mechanical properties of $CoSb_3$ composites, J Mater Eng Perform. 22 (2013) 3561–3565. https://doi.org/10.1007/s11665-013-0641-9.

[26] H. Yin, S. Johnsen, K.A. Borup, K. Kato, M. Takata, B.B. Iversen, Highly enhanced thermal stability of Zn_4Sb_3 nanocomposites, Chemical Communications. 49 (2013) 6540–6542. https://doi.org/10.1039/c3cc42340a.

[27] D.B. Xiong, N.L. Okamoto, H. Inui, Enhanced thermoelectric figure of merit in p-type Ag-doped ZnSb nanostructured with Ag_3Sb, Scr Mater. 69 (2013) 397–400. https://doi.org/10.1016/j.scriptamat.2013.05.029.

[28] L. Bjerg, G.K.H. Madsen, B.B. Iversen, Enhanced thermoelectric properties in zinc antimonides, Chemistry of Materials. 23 (2011) 3907–3914. https://doi.org/10.1021/cm201271d.

[29] A. Ostovari Moghaddam, A. Shokuhfar, Y. Zhang, T. Zhang, D. Cadavid, J. Arbiol, A. Cabot, Ge-Doped ZnSb/β-Zn_4Sb_3 Nanocomposites with High Thermoelectric Performance, Adv Mater Interfaces. 6 (2019) 1–8. https://doi.org/10.1002/admi.201900467.

[30] L.T. Zhang, M. Tsutsui, K. Ito, M. Yamaguchi, Effects of ZnSb and Zn inclusions on the thermoelectric properties of β-Zn_4Sb_3, J Alloys Compd. 358 (2003) 252–256. https://doi.org/10.1016/S0925-8388(03)00074-4.

[31] D. Eklof, A. Fischer, Y. Wu, E.-W. Scheidt, W. Scherer, U. Haussermann, Transport properties of the II – V semiconductor ZnSb, J Mater Chem A. 1 (2013) 1407–1414. https://doi.org/10.1039/c2ta00509c.

[32] G. Zhu, W. Liu, Y. Lan, G. Joshi, H. Wang, G. Chen, Z. Ren, The effect of secondary phase on thermoelectric properties of Zn_4Sb_3 compound, Nano Energy. 2 (2013) 1172–1178. https://doi.org/10.1016/j.nanoen.2013.04.010.

[33] J. Yang, G. Liu, Z. Shi, J. Lin, X. Ma, Z. Xu, G. Qiao, An insight into β-Zn_4Sb_3 from its crystal structure, thermoelectric performance, thermal stability and graded material, Mater Today Energy. 3 (2017) 72–83. https://doi.org/10.1016/j.mtener.2017.02.005.

[34] R. Pothin, R.M. Ayral, A. Berche, F. Rouessac, P. Jund, Interest of the differential thermal analysis on the characterization of a thermoelectric material: ZnSb, J Alloys Compd. 657 (2016) 358–365. https://doi.org/10.1016/j.jallcom.2015.10.118.

[35] P. Balasubramanian, M. Battabyal, A. Chandra Bose, R. Gopalan, Effect of ball-milling on the phase formation and enhanced thermoelectric properties in zinc antimonides, Mater Sci Eng B Solid State Mater Adv Technol. 271 (2021) 115274. https://doi.org/10.1016/j.mseb.2021.115274.

[36] D. Sidharth, B. Srinivasan, A.S.A. Nedunchezhian, P. Thirukumaran, M. Arivanandhan, R. Jayavel, Enhancing the thermoelectric performance of nanostructured ZnSb by heterovalent bismuth substitution, Journal of Physics and Chemistry of Solids. 160 (2022) 110303. https://doi.org/10.1016/j.jpcs.2021.110303.

[37] C. Li, G. Wang, D. Qi, D. Shi, X. Zhang, H. Wang, Suppression for an intermediate phase in ZnSb films by NiO-doping, Sci Rep. 7 (2017) 2–9. https://doi.org/10.1038/s41598-017-09338-3.

[38] M. Tedjani, Thermoelectric Properties of $SrTi_{(1-x)}Zr_{(x)}O_3$ Alloys: a First-Principle Study, J Supercond Nov Magn. 34 (2021) 2479–2484. https://doi.org/10.1007/s10948-021-05935-6.

[39] W. liu, X. Yan, G. Chen, Z. Ren, Recent advances in thermoelectric nanocomposites, Nano Energy. 1 (2012) 42–56. https://doi.org/10.1016/j.nanoen.2011.10.001.

[40] Y. Lin, M. Wood, K. Imasato, J.J. Kuo, D. Lam, A.N. Mortazavi, T.J. Slade, S.A. Hodge, K. Xi, M.G. Kanatzidis, D.R. Clarke, M.C. Hersam, G.J. Snyder, Expression of interfacial Seebeck coefficient through grain boundary engineering with multi-layer graphene nanoplatelets, Energy Environ Sci. 13 (2020) 4114–4121. https://doi.org/10.1039/d0ee02490b.

[41] J. de Boor, On the applicability of the single parabolic band model to advanced thermoelectric materials with complex band structures, Journal of Materiomics. 7 (2021) 603–611. https://doi.org/10.1016/j.jmat.2020.10.013.

[42] Y.Y. Li, X.Y. Qin, D. Li, J. Zhang, C. Li, Y.F. Liu, C.J. Song, H.X. Xin, H.F. Guo, Enhanced thermoelectric performance of $Cu_2Se/Bi_{0.4}Sb_{1.6}Te_3$ nanocomposites at elevated temperatures, Appl Phys Lett. 108 (2016) 062104. https://doi.org/10.1063/1.4941757.

[43] B. Jabar, X. Qin, D. Li, J. Zhang, A. Mansoor, H. Xin, C. Song, L. Huang, Achieving high thermoelectric performance through constructing coherent interfaces and building interface potential barriers in n-type $Bi_2Te_3/Bi_2Te_{2.7}Se_{0.3}$ nanocomposites, J Mater Chem A Mater. 7 (2019) 19120–19129. https://doi.org/10.1039/c9ta05798f.

[44] S. Ghosh, S.M. Valiyaveettil, G. Shankar, T. Maity, K.H. Chen, K. Biswas, S. Suwas, R.C. Mallik, Enhanced Thermoelectric Properties of In-Filled Co_4Sb_{12} with InSb Nanoinclusions, ACS Appl Energy Mater. 3 (2020) 635–646. https://doi.org/10.1021/acsaem.9b01851.

[45] S. Ghosh, G. Shankar, A. Karati, K. Werbach, G. Rogl, P. Rogl, E. Bauer, B.S. Murty, S. Suwas, R.C. Mallik, Enhanced Thermoelectric Performance in the $Ba_{0.3}Co_4Sb_{12}$/InSb Nanocomposite Originating from the Minimum Possible Lattice Thermal Conductivity, ACS Appl Mater Interfaces. 12 (2020) 48729–48740. https://doi.org/10.1021/acsami.0c17254.

[46] S. Ghosh, G. Shankar, A. Karati, G. Rogl, P. Rogl, E. Bauer, B.S. Murty, S. Suwas, R.C. Mallik, Preferential phonon scattering and low energy carrier filtering by interfaces of: In situ formed InSb nanoprecipitates and GaSb nanoinclusions for enhanced thermoelectric performance of $In_{0.2}Co_4Sb_{12}$, Dalton Transactions. 49 (2020) 15883–15894. https://doi.org/10.1039/d0dt03429k.

[47] D. Zhao, J. Ning, D. Wu, M. Zuo, Enhanced thermoelectric performance of Cu_2SnSe_3-based composites incorporated with nano-fullerene, Materials. 9 (2016) 629. https://doi.org/10.3390/ma9080629.

[48] L. Zhao, L. Yu, J. Yang, M. Wang, H. Shao, J. Wang, Z. Shi, N. Wan, S. Hussain, G. Qiao, J. Xu, Enhancing thermoelectric and mechanical properties of p-type Cu_3SbSe_4-based materials via embedding nanoscale Sb_2Se_3, Mater Chem Phys. 292 (2022) 126669. https://doi.org/10.1016/j.matchemphys.2022.126669.

[49] C.K. Lin, M.S. Chen, R.T. Huang, Y.C. Cheng, P.Y. Lee, Thermoelectric properties of alumina-doped $Bi_{0.4}Sb_{1.6}Te_3$ nanocomposites prepared through mechanical alloying and vacuum hot pressing, Energies (Basel). 8 (2015) 12573–12583. https://doi.org/10.3390/en81112323.

[50] H.S. Kim, Z.M. Gibbs, Y. Tang, H. Wang, G.J. Snyder, Characterization of Lorenz number with Seebeck coefficient measurement, APL Mater. 3 (2015) 1–6. https://doi.org/10.1063/1.4908244.

[51] C. Chubilleau, B. Lenoir, P. Masschelein, A. Dauscher, C. Candolfi, E. Guilmeau, C. Godart, Influence of ZnO nano-inclusions on the transport properties of the CoSb3 skutterudite, J Alloys Compd. 554 (2013) 340–347. https://doi.org/10.1016/j.jallcom.2012.11.167.

[52] P. Puneet, R. Podila, M. Karakaya, S. Zhu, J. He, T.M. Tritt, M.S. Dresselhaus, A.M. Rao, Preferential scattering by interfacial charged defects for enhanced thermoelectric performance in few-layered n-type Bi_2Te_3, Sci Rep. 3 (2013) 3212. https://doi.org/10.1038/srep03212.